Predictions and measurements of mass spectra of the charged nucleonic component of cosmic rays at mountain altitude

H. B. Barber, T. Bowen, D. A. Delise,* E. W. Jenkins, J. J. Jones, R. M. Kalbach,† and A. E. Pifer
Department of Physics, The University of Arizona, Tucson, Arizona 85721
(Received 13 June 1980)

A cosmic-ray mass spectrometer utilizing a superconducting magnet, digitized wire spark chambers, and time-of-flight scintillation counters has examined the mass spectrum of low-momentum charged particles at 2750-m altitude (747 g/cm^2). For the first time at mountain altitude, the deuteron spectrum has been clearly resolved. The proton results confirm earlier work. The data indicate the presence of a few ^{4}He nuclei. Upper limits are given to fluxes of antiproton and hypothetical massive particles in the 5-to-10-GeV/c^2 range. The low-momentum deuteron spectrum, as well as the proton spectra at various atmospheric depths, can be well understood in terms of a cosmic-ray atmospheric cascade calculation. The deuterons are principally produced by $N + N \rightarrow d + \pi$ and quasielastic nucleon scattering on n-p pairs within the nucleus. Calculations are also presented of the expected intensities of low-momentum antiprotons and hypothetical massive particles at mountain altitude.

INTRODUCTION

Although historically many of the elementary particles were first discovered in the cosmic radiation, few experiments have examined the mass spectrum of statistically large numbers of cosmic-ray charged particles. The proton component of cosmic rays is important at all altitudes, but little is known of the spectra of deuterons and other light fragments from nuclear intereactions in the atmosphere.[1,2] The antiproton component, which must be present, has eluded cosmic-ray physicists, except for one event,[3] until the recent results of Golden *et al.*[4] Experiments which detect energetic penetrating showers with large time delays relative to an extensive-air-shower front indicate the possible existence of heavy long-lived hadrons.[5-8]

A number of mass-sensitive experiments have been carried out which utilize the energy-loss rate and range, setting intensity limits for massive singly charged nonrelativistic particles in the region of 10^{-8}–10^{-9} cm^{-2} sec^{-1} sr^{-1}.[9-11] These experiments are characterized by broad mass resolution and large amounts of material in the detection path; hence these experiments would be most sensitive for particles having long nuclear-interaction mean free paths.

A magnetic-mass-spectrometer search for massive particles was carried out by Kasha and Stefanski.[12] They examined particles arriving at sea level with a zenith angle of 75°; this inclination was chosen so that the hypothetical massive particles produced in the upper atmosphere would be slowed down to nonrelativistic velocities by the 4000 g/cm^2 of air along the particle path. This experiment set an upper intensity limit of 2.4 $\times 10^{-8}$ cm^{-2} sec^{-1} sr^{-1} for momenta from 0.5 M_X to 1.1 M_X ($\beta = 0.5$ to 0.75). They attributed the four events which passed all selection criteria and which gave masses of 3.1, 10.0, 12.5, and 12.7 GeV/c^2 to background, since they estimated one might expect five background events.

Following several search experiments for fractionally charged particles,[13-16] the Arizona group constructed a superconducting-magnet mass spectrometer to study the mass spectrum of vertically incident cosmic ray particles at mountain altitude. The objectives were to study the spectra of protons, deuterons, and other nuclear fragments, to carry out a massive-particle search under conditions complementary to those of Kasha and Stefanski, and to begin the development of techniques which might eventually permit detection and study of cosmic-ray antiprotons.

SITE

The University of Arizona Cosmic Ray Laboratory is near the summit of Mt. Lemmon in the Santa Catalina Mountains, about 72 km by road north of The University of Arizona. This site has year-round accessibility at an altitude of 2750 m which corresponds to an atmospheric depth of 747 g/cm^2 and has a geomagnetic vertical cutoff rigidity of 5.59 GV.[17]

APPARATUS

The University of Arizona cosmic-ray mass spectrometer, shown schematically in Fig. 1, determines the rigidity of an entering charged cosmic-ray secondary by measuring its deflection θ in the field of a superconducting magnet. Track delineation is by wire spark chambers (SC1 to SC6). The velocity ($\beta = v/c$) is determined by measuring times of flight between pairs of scintilla-

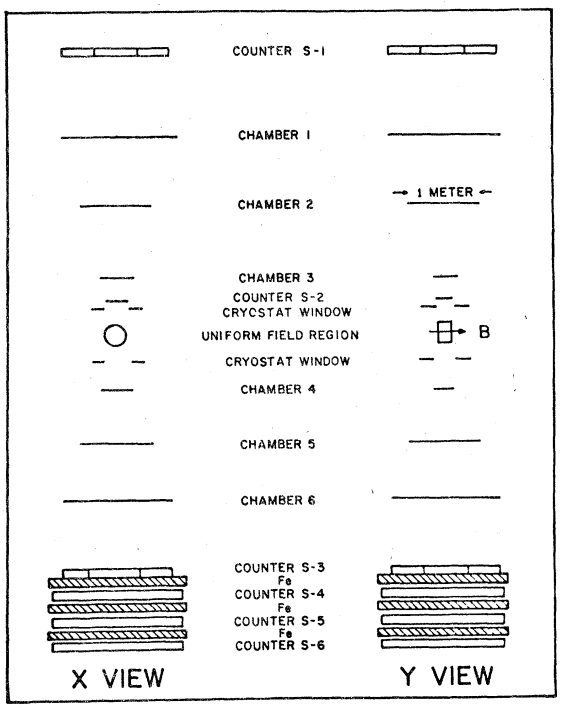

FIG. 1. Diagram of apparatus. Chambers 1–6 are spark chambers, S1–S6 are scintillation counters. The y-axis alignment is approximately north-south.

tion counters (S1-S3, S1-S2), and the charge state (Q = number of unit charges) of the particle is found by measuring the energy deposited in S1. The momentum is given experimentally by

$$P = \frac{Q \int B\, dl}{\theta} \tag{1a}$$

$$\cong \frac{0.07Q}{\theta}\ \mathrm{GeV}/c\ , \tag{1b}$$

where P is the momentum in GeV/c, θ is the bend angle in radians, and $\int B\, dl/\theta$ is the rigidity. The particle rest mass M_0 in GeV/c^2 is given by

$$M_0 = P/\beta\gamma c\ ,$$

where

$$\gamma = (1-\beta^2)^{-1/2}\ , \tag{2}$$

and the momentum P is in GeV/c. Various parts of this apparatus will be considered separately.

Superconducting magnet

The magnet is composed of two coils of rectangular cross section (27.2 cm inside diameter, 48.3 cm outside diameter, 7.1 cm thick) which are aligned axially and have a free space between them of 19.05 cm to make a uniform central field region. The superconductor is niobium titanium in a copper matrix with a 3:1 copper to superconductor ratio. The magnet contains a superconducting switch which allows the magnet to be charged to a given current, then switched into a persistent current mode in which it is isolated from any external power supply. In the persistent mode nonsuperconducting parts of the current path, such as solder contacts and copper in the connections to the superconducting switch, cause the magnet's current to decay with a time constant of 52.4 days. The data to be analyzed here were taken at a current of 100 A at which the axial field was 7.7 kG and the field integral was approximately 2 kG m.

Since the mass resolution depends strongly on the multiple scattering in the magnet region (see Appendix A), care was taken to allow as little material as possible in the particle path. Entry and exit windows to the vacuum region were of 0.25-mm Mylar, the heat shield had windows of 0.025-mm aluminum, and there were 18 layers of 0.00825-mm aluminized Mylar superinsulation in the vacuum region. The total amount of matter a particle encountered in traversing the magnet amounted to approximately 0.2 g/cm^2.

During the operation of the magnet, boiloff was 0.97 l/h for liquid helium and about 2 l/h for liquid nitrogen. Since liquid-helium cost was a major factor in the experiment operating expense, helium was reclaimed by a gas recovery system, reliquified, and recycled. The magnet was cooled down at the University of Arizona Physics Liquifier Facility, transported while cold, and energized at the mountain site.

Wire spark chambers

Track delineation was accomplished by six wire spark chambers with magnetostrictive readout shown in Fig. 1. Spark-chamber dimensions were: 1.5 m × 1.5 m for chambers 1 and 6; 1 m × 1 m for chambers 2 and 5; and 0.27 m × 0.43 m for chambers 3 and 4 with the larger dimension perpendicular to the magnetic-field direction. All chambers had 1-cm gaps with 10 aluminum wires/cm for the two large chambers and 20 copper wires/cm for the other chambers. The wire planes were separated from the atmosphere by 0.0508-mm Mylar windows. A gas composed of 20% He and 80% Ne was constantly circulated through each chamber by a gas delivery, purification, and recirculation system, which allowed introduction of small amounts of ethyl alcohol for quenching purposes.

The chamber-pulsing system was composed of an avalanche transitor-triggered spark gap which in turn triggered separate 5C22 hydrogen thyratron pulsers mounted on each spark chamber (see Fig. 2). Two sets of two adjacent wires on opposite ends of each wire plane were used as fiducial wires and connected to a separate high-voltage

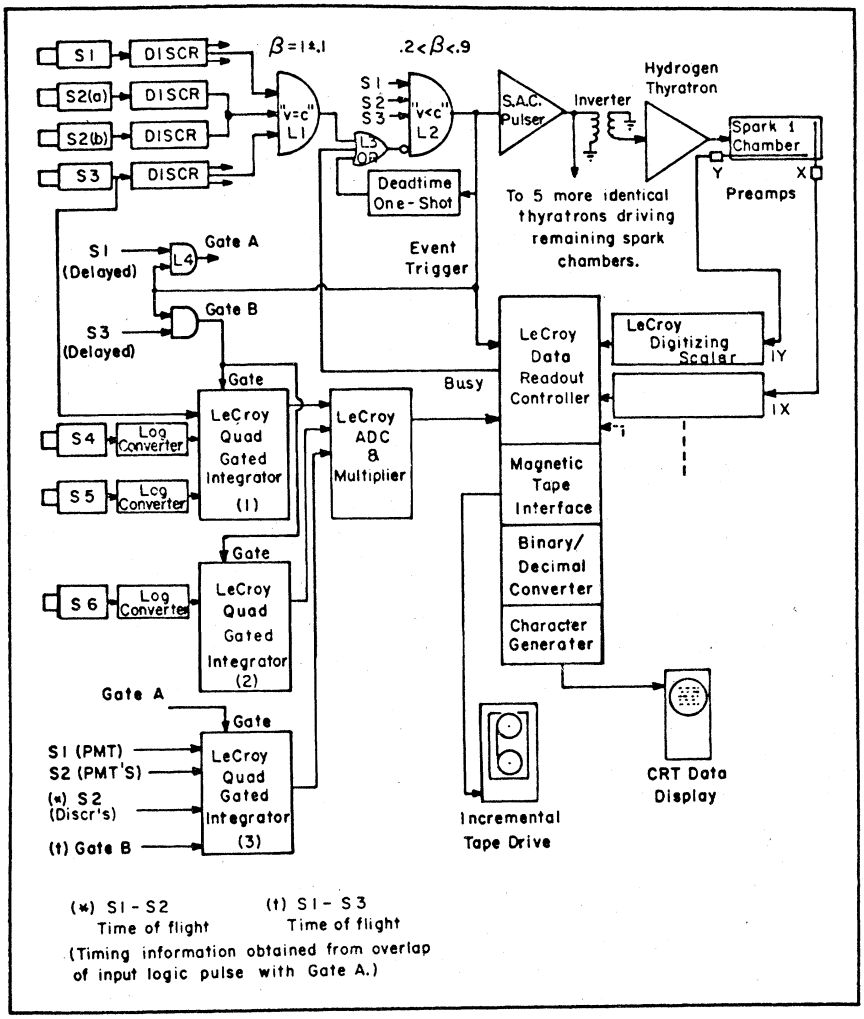

FIG. 2. Schematic diagram of the electronics.

pulsing system. The magnetostrictive readout was digitized by scalers driven by a 20-MHz clock.[18] Each channel had two scalers, so the positions of up to two sparks per chamber were recorded.

Spark-chamber operation seemed less reliable at mountain altitude as compared to sea level; satisfactory operation was very dependent upon high gas purity. The magnetostrictive wands had to be restroked with a permanent magnet every few hours. Due to low spark-chamber efficiency, the overall efficiency was 55% for obtaining two x coordinates above the magnet and two below for the bend angle as well as three collinear y coordinates.

Scintillation counters and time-of-flight system

The time-of-flight system was composed of three scintillation counters $S1$, $S2$, and $S3$, shown in Fig. 1. The time differences between $S1$ and $S3$ (T_1) and between $S1$ and $S2$ (T_2) were measured and recorded independently.

Counters $S1$ and $S3$ were 13-cm-thick liquid scintillation counters of octagonal cross section 152 cm across the faces. The liquid scintillator was 1,2,4-trimethyl benzene in a toluene base,[19] which has a light output 80% of anthracene and a decay constant of 2.7 nsec. Owing to the fact that the scintillator is both volatile and poisoned by oxygen, the counter was made gas tight and the container was continuously purged with dry nitrogen. The counter was constructed with inert materials such as metals, teflon, and polyethylene to avoid attack by toluene. The liquid was viewed from a vertical distance of 60 cm by a 5-in.-diameter photomultiplier tube with a bialkali photocathode, a rise time of 2.7 nsec, and an average

transit time of approximately 100 nsec with low jitter.[20]

Counter $S2$ was a 20 cm × 33 cm plastic scintillator 0.519 cm thick and was located immediately above the magnet entrance window. The scintillator, chosen to be as thin as possible to reduce the multiple scattering, was viewed at each end by a standard 2-in. photomultiplier tube. To remove these tubes from the high magnetic-field region, they viewed the scintillator through 1-m-long adiabatic light guides.

The shortest time of flight for T_1, for a particle traveling at the speed of light ($v=c$ or $\beta=v/c=1$), was 24.0 nsec. In practice the measured time fluctuates due to light transit time in the counters, different trajectory lengths, jitter in the photomultiplier tubes, and various other factors such as scintillator fluorescence statistics and the characteristics of the electronics. The system was designed so that the standard deviation of these fluctuations did not exceed 2.5 nsec. This then allows T_1 to be used as a trigger with a cutoff of $\beta=0.9$. It should be noted that, since each particle trajectory was eventually determined during data analysis, the contribution to the above errors due to light transit time in the counters and trajectory length were calculated and corrected, reducing the time litter to 0.9 nsec thereby allowing the velocity to be determined to much higher precision for mass determination. The availability of two times of flight per event facilitated rejection of background events.

Auxiliary counters

Subsidiary information about each event was available from a range counter system beneath $S3$; this information was used in the tuneup of the apparatus, but was not used in the data analysis. The range counter system was composed of three 1.8 m × 1.8 m liquid scintillation counters, $S4$, $S5$, and $S6$, alternating with layers of iron absorber as shown in Fig. 1. The counters were described in an earlier experiment.[21] The top layer of iron was 13 cm thick and the other two layers were each 10 cm.

Electronics

A diagram of the electronics is shown in Fig. 2. Pulse widths which affected time-of-flight measurements were set by clipping lines to ensure stability. The input pulses to coincidence units $L1$ and $L2$ are shown in Fig. 3(a) for the case where $v=c$ ($\beta=1$), and in Fig. 3(b) for the case where $v=c/3$ ($\beta=\frac{1}{3}$). In Fig. 3(a), the presence at $L2$ of an anticoincidence input pulse, which is

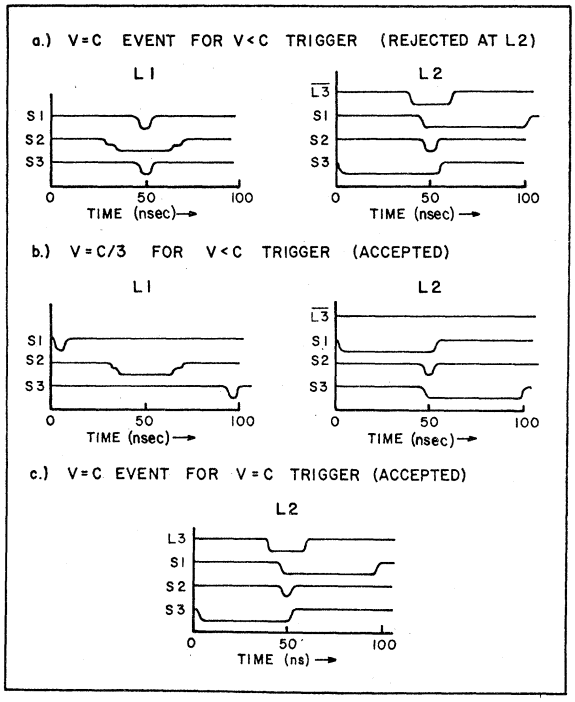

FIG. 3. Examples of pulse timing for various trigger conditions.

the output of $L1$ via $L3$, suppresses the output of $L2$ for all events with v close to c. How close v is to c is determined by the widths of pulses $S1$ and $S3$ into $L1$. These widths were chosen so that all events with $v \geq 0.9c$ ($\beta \geq 0.9$) were rejected. This configuration is referred to as the $v<c$ trigger. If the $L1$ input cable to $L3$ is removed (see Fig. 2), the $v=c$ anticoincidence is not available to $L2$ so that all events are allowed. This configuration is called the $v \leq c$ trigger. To obtain only the $v=c$ events, $L1$ input cable to $L3$ is placed on the fourth coincidence input to $L2$ so that $L2$'s input resembles Fig. 3(c). For T_1 the maximum time of flight (smallest β) is determined in the case of the $v<c$ and $v \leq c$ by the sum of the length of pulses $S1$ and $S2$ entering $L2$ [Fig. 3(b)]. This length was chosen as 120 nsec somewhat arbitrarily, to allow triggering for the slowest protons not bent out of the solid angle acceptance of the spectrometer. The event trigger (output of $L2$) was placed in coincidence with $S1$'s discriminator pulse ($L4$) to provide a gate with the timing of $S1$ for quadintegrator 3. Properly delayed discriminator pulses from counters $S2$ and $S3$ were then introduced into quadintegrator 3, where the overlap of these pulses with the gate pulse was a measure of the time delay between the counters, i.e., the time of flight. T_1 was the time delay between $S1$ and $S3$ and T_2 was

that between $S1$ and $S2$. The two other input channels of quadintegrator 3 were used for raw phototube pulses from counters $S1$ and $S3$, which, when integrated, measured the energy deposited in the scintillator and hence indicated the charge of the particle traversing the counter. Two other quadintegrators, 1 and 2, were available to provide other pulse-height information.

The event trigger fired the spark chambers and initiated the readout cycle. The time delay from the event trigger to the firing of a given spark chamber was from 250 to 400 nsec depending on the chamber. In order to prevent spark rf noise or a subsequent event from changing the data before they could be read out, the event logic ($L2$) was gated off for 1.5 μsec until the controller took over the readout cycle. The controller serially interrogated the spark-chamber scalers, the data scalers, and the quadintegrators, after digital conversion of their data by an analog-to-digital converter, and then sent these data over a data bus to the magnetic tape interface which controlled its readout onto magnetic tape by an incremental recorder. The entire data-readout cycle, including the time to write on the tape, took 0.96 sec. During this time, the controller gated off the event logic ($L2$) to prevent accumulation of new data. The incremental recorder wrote 57 24-bit words for each event.

The step shape of the pulse which is the $S2$ input to coincidence unit $L1$ in Fig. 3(a) and (b) has no effect on its operation and arises from the addition of the discriminator outputs of the two $S2$ photomultiplier tubes in the case in which one photomultiplier fires earlier than the other because the particle transited the plastic scintillator nearer to the tube. Assuming that the two discriminator outputs are equal, this procedure effectively averages the time determinations of the two photomultiplier tubes, since it is the overlap of this step-shaped pulse with the gate pulse in quadintegrator 3 which measures $T2$.

GEOMETRY FACTOR

Since the geometry factor is affected by the bending of trajectories, it is a function of the momentum. Because the bend angle θ scales as the ratio of the magnet current to momentum (I/p), the acceptance need only be determined for one magnet current I. It should also be noted that θ decreases for increasing momentum so that in the limit of high momentum the spectrometer appears as simply an array of detectors, as in the zero-field case.

Monte Carlo calculations are well suited for calculating the geometry factor when complicated counter shapes ($S1$ and $S3$ are octagonal) are involved. The Monte Carlo program AOMEGA was adapted for our geometry from one by Crannell and Ormes,[22] which was designed for an arbitrary number of parallel detectors of rectangular cross section. AMOEGA found the area times solid angle acceptance for zero field to be $A\Omega_{p\to\infty} = 32.32 \pm 0.44$ cm^2/sr, where the error is statistical. For nonzero magnet current a trajectory tracing program was incorporated, and each particle was traced through the field region while being required to remain within the magnet fiducial region. The geometry factor, as a function of momentum, $A\Omega(p)$, is shown in Fig. 4, as a function of momentum, where the errors are statistical with 10^5 Monte Carlo particles per momentum.

DATA REDUCTION

With the exception of a few calibration runs, all the data considered here were taken during January 1974, and consisted of 24 magnetic tapes with between 18 000 and 30 000 events on each tape.

Preliminary analysis

In order to facilitate utilization of the data by The University of Arizona Computer Center's CDC 6400, a program called REPACK was written which read data off a raw data tape, rejected unusable events, and wrote the good events on a second tape in a denser format. REPACK rejected events with short records, unreadable records, both time-of-flight numbers equal to zero, or no spark in either chamber 4 or 5. The latter condition was chosen to simplify data reduction, because chamber 6 had a very low efficiency and two chambers were needed on each side of the

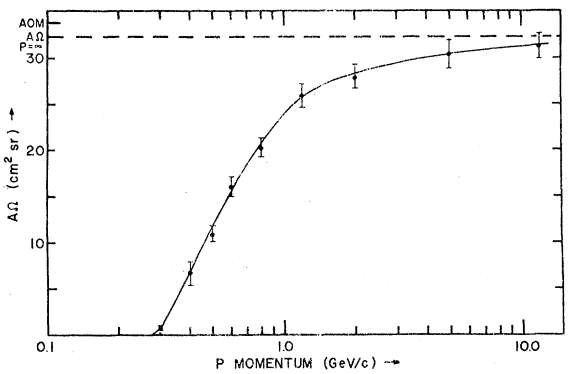

FIG. 4. Area–solid-angle product ($A\Omega$) of the spectrometer as a function of particle momentum. Data is from the Monte Carlo calculation of Appendix B for a magnet current of 100 A.

magnet in the x projection. This procedure resulted in the loss of less than 4% of the good data. Excluding calibration data and periods of electronic or magnet malfunction, 11 tapes were left for data reduction, totaling 239 436 triggers. The disposition of these triggers, with respect to type and whether the magnet was on or off, is shown in Table I. Of the 173 612 $v<c, I=100$ A triggers, 133 155 (77%) survived the scrutiny of REPACK. The $v<c$, $I=0$ triggers were not analyzed.

Trajectory determination

A program called GUTS was developed to arrange the various spark-chamber spark coordinates into possible particle tracks, and to determine from these the most probable trajectory. Since each spark chamber was composed of a single pair of wire planes with wires oriented at right angles, it was necessary to consider the x and y projections separately. Two possible sparks per projection, with two projections, allows a twofold ambiguity in the pairing of x and y plane sparks when two particles transit the chamber simultaneously. Fortunately, the resolution of the ambiguity was unnecessary. Since the magnetic field direction was perpendicular to the x axis (see Fig. 1), the bending of the trajectory was almost entirely in the x-z plane. Of course, the y-z projection of the trajectory was still necessary for reconstructing the particle trajectory since the field strength and, hence, path integral varied with y position. Only the broadest cuts were made in the data using y projection values for this reason. In practice, an error in the choice of which tracks were associated in x and y projections results in a small error in $\int B\,dl$ and, hence, the momentum determination, thus broadening the mass peak.

In the x projection, separate straight line tracks were found for the three chambers above the magnet (top set) and the three chambers below the magnet (bottom set). Each set was searched first for three spark tracks, then for two-spark tracks. The impact parameter, defined as the closest distance from the extended track to the center of symmetry of the magnet in the x projection, was determined for each track in both sets of chambers. Any track was rejected that had an impact parameter greater than 35.6 cm, a radius associated with internal magnet clearances. GUTS then considered up to ten probable pairs, i.e., combinations of top and bottom tracks. Since the magnetic field had rotational symmetry in the x projection and was approximately constant as a function of y in the central field region, and since also the field strength dropped off quickly as a function of distance from the magnet region, the impact parameter was an approximately conserved quantity. For a track pair to be considered probable, the difference between impact parameters was required to be less than 2.0 cm. If no pair satisfied this criterion, the event was rejected. The pair of tracks with the smallest impact parameter difference (Δb) was chosen as the most probable trajectory.

TABLE I. Data summary.

Trigger	Zero field ($I=0$)	Field on ($I=100$ A)
$v\simeq c$	17 239 triggers	16 404 triggers
$v<c$	32 181 triggers	173 612 triggers

In the y projection, all six spark chambers were considered together, and straight-line tracks were searched for by the method of stringing.[23] Each acceptable track candidate transited the magnet entirely within the fiducial region and had at least three sparks with at least one spark on either side of the magnet. GUTS stored up to ten such tracks, each of whose χ^2 was found from a least-squares-fit subroutine. Only tracks with χ^2 less than ten were deemed acceptable. The most probable y trajectory was then the member of the set of tracks with the largest number of sparks that had the smallest χ^2. If no acceptable track was found, the event was rejected.

Spark-chamber-alignment resolution and efficiency

Before further reduction of the data could proceed, the relative positions of the spark chambers had to be determined. Since zero-field ($I=0$) events with $v=c$ should be straight lines in both x and y projections, they were used to determine the errors in chamber alignment. Such events defined by two chambers were used to calculate the expected position of a spark in each of the other chambers. The difference between the actual position and this expected spark position as determined from the best-fit track was histogrammed. The displacements from zero of the histogram peaks determined the corrections to the chamber positions. The widths of these peaks measured the spark chamber resolution while the relative number of events in each peak measured the chamber efficiency (Table II). Chambers 1 and 6 had twice the wire spacing of the others as indicated by the resolutions in Table II while the low y efficiency of chamber 6 precluded determination of its y resolution.

Using GUTS on the $v=c$ zero-field data, a his-

TABLE II. Wire-spark-chamber resolution and efficiencies.

Chamber	1	2	3	4	5	6
x resolution	2.1 mm	0.8 mm	0.6 mm	1.3 mm	0.7 mm	1.1 mm
y resolution	3.3 mm	1.4 mm	1.6 mm	1.4 mm	1.4 mm	
x efficiency	16%	91%	98%	91%	86%	42%
y efficiency	44%	82%	77%	77%	81%	2%

togram of bend angles between top and bottom tracks was obtained, the width of which was a measure of angular measurement precision. Momentum resolution could then be found using Eq. (2). The resulting maximum detectable momentum = 31.3 GeV/c is consistent with both the resolutions of Table II and the results of Appendix A.

$v=c$ field-energized data

GUTS was applied to the $v=c$ data with the field energized ($I=100$ A). A histogram of impact-parameter differences Δb between top and bottom tracks in the x projection had a Gaussian distribution with full width of half maximum = 0.5 cm, verifying the conservation of impact parameter and the choice of cut at $\Delta b = \pm 2$ cm. A histogram of bend angle between top and bottom tracks (x projection) had a plus-to-minus asymmetry consistent with the magnitude of the muon charge asymmetry[24,25] under the assumption that these events were predominantly low energy muons. The shape of this bend-angle distribution was consistent with the muon spectral index.[26]

$v<c$ data and field tracing

The 133 155 $v<c$, field-energized ($I=100$ A) events surviving REPACK were processed by GUTS to yield 30 782 events with acceptable trajectories in both x and y projections. In order to determine the mass to high precision, it was necessary to accurately determine the rigidity by finding the path-dependent field integral $\int B\,dl$ for each event individually.

The magnetic field was modeled by a computer program called MAGNET, which broke up each coil into a large number of discrete current loops and summed the off-axis contribution of each of these current loops to the magnetic field at any point in the vicinity of the magnet. During a magnet test at a current of 150 A, the magnetic field was measured on axis at the outer face of the Dewar using a Hall probe gaussmeter. This result when compared to a later calculation using MAGNET agreed to within 1%, the expected gaussmeter accuracy. MAGNET was used to generate a field map for a fiducial region set by the magnet clearances, and this map was stored on magnetic tape.

Using this field map, a first estimation of the rigidity from the bend angle in the x projection, and Eq. (1), another program, BEND, traced the particle through the magnetic field region, determining its exit direction.[27] BEND then compared the exit slope to that of the observed trajectory and corrected the rigidity accordingly. Two iterations of this procedure yielded the measured rigidity for that event. A test with constructed events of known rigidity showed that this process was capable of retrieving the rigidity with an accuracy greater than 1%. An event which exited the magnet fiducial region at any step of this process was rejected. BEND found satisfactory rigidity for 23 350 of the $v<c$, $I=100$ A events.

Time-of-flight corrections

For a particle transiting two counters A and B, the velocity is given by

$$\beta = \frac{Z}{Z + 29.98(\tau - \tau_A + \tau_B)}, \tag{3}$$

where Z is the trajectory length between A and B measured in cm, τ is the measured time of flight in excess of that required by a $v=c$ particle (hereafter referred to as the time of flight), τ_A and τ_B are the light transit times in counters A and B measured in nsec, and 29.98 is the velocity of light in units of cm/nsec.

Time-of-flight comparison

An analysis[26] showed no advantage to averaging T_1 and T_2, but a comparison of them was useful in eliminating false triggers. A false trigger corresponded to a particle or spurious electronic pulse triggering $S1$ followed by another particle, usually a muon, transiting the apparatus as a valid event with the delay between them interpreted as a time of flight (T_1). Of course, T_2 would not yield a consistent result in this case. Consider a time-of-flight system with counter separation Z_i (cm), time-of-flight excess, τ_1 (nsec), and velocity given by

$$\beta_i = \frac{Z_i}{Z_i + 29.98\tau_i}. \tag{4}$$

Differentiation with respect to τ_i yields

$$d\beta_i = \beta_i^2 \frac{29.98}{Z_i} d\tau_i , \quad (5)$$

indicating that the error in the velocity is proportional to the velocity squared. A statistical analysis of velocity error originating from timing jitter in the various photomultiplier tubes indicated[26] a sufficient acceptance criterion for the data cut to be

$$|\beta_1 - \beta_2| \leq 0.0905\beta_1^2 , \quad (6)$$

where β_1 and β_2 correspond to T_1 and T_2, respectively.

Preliminary mass distributions

Preliminary mass distributions for $Q > 0$ and $Q < 0$ for $v < c$ data were obtained using T_1 only, and the $Q > 0$ distribution showed a prominent peak verifying data analysis up to this point. Proton peak positions for various data tapes and velocity intervals were useful in determining the magnet current decay correction and time-of-flight zero.[26]

Charge determination

Position-dependent corrections to the pulse height were determined for the better counter, *S*1, using minimum-ionizing muons. Corrected *S*1 mean pulse heights were then found for protons in various momentum intervals. The result, as a function of the corresponding proton specific energy losss, $-dE/dx$,[26,28] shown in Fig. 5, indicated saturation effects for large specific energy loss. The solid curve in Fig. 5 shows the relationship which was assumed for use in distinguishing particle charge ($Q^2 = 1$ or 4). In ambiguous cases $Q^2 = 1$ was assumed.

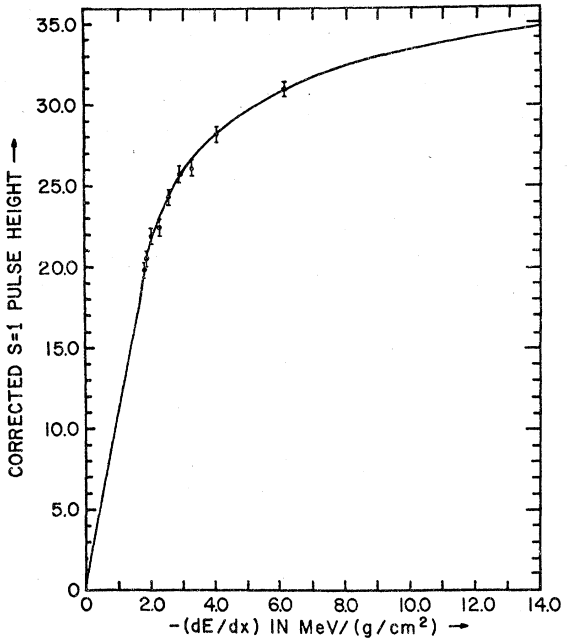

FIG. 5. Corrected pulse height vs specific energy loss for counter *S*1. The plotted points were calculated from dE/dx of protons with known momentum. The solid curve was used for estimating charge.

RESULTS

Final mass spectra were determined for various experimental parameters. Figure 6 shows samples of mass spectra for charges $Q = \pm 1, \pm 2$, in ten intervals of velocity with the time-of-flight cut given by Eq. (6). The data used to generate these histograms were corrected for magnet-field decay and had an impact-parameter difference $|\Delta b| \leq 1.0$ cm. However, the data which are plotted in Fig. 6(a) for the velocity interval $0.20 < \beta \leq 0.35$ does not have the time-of-flight cut because of the low background. In all the histograms the interval on the abcissa is the logarithm of the mass in units of the nucleon mass divided by charge, because this quantity has more nearly symmetrical errors than the mass itself. Mass divided by charge is used since it is proportional to rigidity, and thus apparatus-dependent effects may appear vertically aligned in the four histograms.

The histograms of Fig. 6 show clean proton peaks with little background except for the higher-velocity intervals. This is characteristic of the data even with many of the cuts relaxed. The $Q = +1$ histograms in Fig. 6 show clear deuteron peaks in the region near twice the nucleon mass. No tritons are evident at three times the nucleon mass. The $Q = -1$ histograms are very clean with no antiproton peaks, and there are no indications of massive $Q = -1$ or $Q = +1$ particles. The peaks in the $Q = +2$ histograms which are aligned vertically with the proton peaks in the $Q = +1$ histograms would appear to be diprotons, taking into account the mass over charge abscissa scale. These are actually spillover from the $Q = +1$ proton peaks due to statistical fluctuations in the pulse height from which the magnitude of the charge is determined. A $Q = +2$ peak also occurs which is vertically aligned with the deuteron peak in the $Q = +1$ histograms in Figs. 6(b)–6(d). Comparison of the relative numbers of events in the peaks in both $Q = +2$ and $Q = +1$ shows that the second $Q = +2$ peak in each case is not totally due to spillover from the deuteron peak in $Q = +1$, and is thus due to real events with $Q = +2$ and a mass of four times the proton mass: α particles (^{4}He).

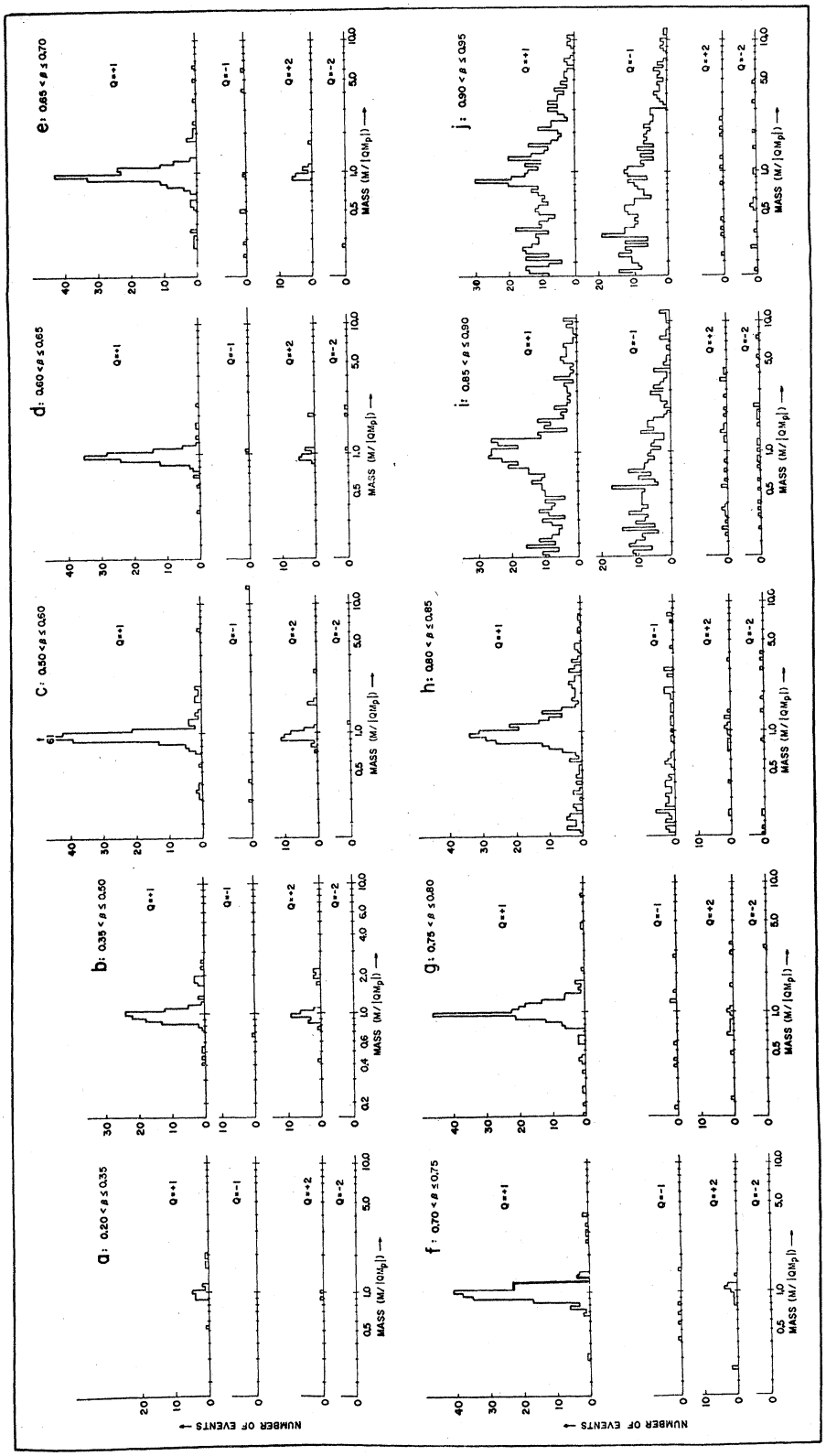

FIG. 6. Mass histograms of corrected $v < c$ data for ten intervals of relativistic velocity β. Only events for which the impact parameter difference Δb and the time-of-flight difference satisfy the conditions $|\Delta b| \leq 1.0$ cm and $|\beta_1 - \beta_2| \leq 0.0905\ \beta_1^2$ are included in these histograms. Choice of the logarithmic abscissa scale of mass divided by charge and proton mass is discussed in the text.

^{3}He events would occur between the spillover proton peak and the α peak in the $Q=+2$ histograms, and there is no evidence of their presence. No peaks corresponding to massive particles are seen in either the $Q=+2$ or $Q=-2$ histograms for any velocity interval.

Slowly moving muons, pions, and electrons are of course present in the cosmic ray secondary spectra but are not expected to show up in these mass spectra because their momenta are too low. For velocities that would trigger the time-of-flight system, bend angles would be too large for them to remain within the solid-angle acceptance of the spectrometer. Charged K mesons might be expected, but owing to their short lifetimes should only appear in the high-velocity interval histograms where background is a problem. All other known elementary particles, both mesons and baryons, have too short a lifetime or are neutral and neither appear nor are expected to appear in these mass spectra. Each of the previously noted possible components will now be discussed separately.

Protons

Mass-spectrum histograms similar to those in Fig. 6, but without the data cuts used to suppress the background, were used to obtain proton absolute intensities. The number of protons in the $M/|Q|=1$, $Q=1$ peak, N_p, was determined for each of ten velocity intervals. The negative charge data in the vicinity of the proton mass, $M/|QM_p|=1$, $Q=-1$, was used for background subtraction. The vertical differential momentum intensities were then calculated from

$$I_p=\frac{N_p}{\Delta p\, A\Omega(p)\Delta t_s \eta}, \tag{7}$$

where N_p is the number of observed protons, Δp is the momentum interval in GeV/c, η is the efficiency for event recognition, Δt_s is the time for which the apparatus was sensitive, and $A\Omega(p)$ is the area times solid-angle acceptance of the spectrometer. The determination of area times solid-angle acceptance, $A\Omega(p)$, which is a function of momentum and the decaying magnet current, is discussed in the section on geometry factor, with the results shown in Fig. 4. Corrections to I_p for this effect are significant for the lower momentum intervals where $A\Omega(p)$ is near threshold (see Fig. 4).

The sensitive time was 3.08×10^5 sec. The event-recognition efficiency, $\eta=0.55$, was determined by considering how the independent inefficiency of each chamber contributes randomly to the probability of observing an event as determined by the track acceptance criteria which were described in the section on trajectory determination. The results for differential proton intensities in the vertical direction are shown in Table III. The intensity in the highest momentum interval has been corrected for selection effects, since the time-of-flight triggering cutoff occurs approximately in the middle of this interval.

Errors in I_p were determined by assuming Poisson statistics for N_p and estimating the probable errors of measurement for other parameters in Eq. (7). The fractional error in $A\Omega(p)$, which is large near threshold in Fig. 4, dominates the error in I_p for low momentum. The error in the product $\eta\Delta t_s$, which is of the order of the error in N_p over most of the momentum range, was estimated by separately analyzing each of nine data tapes.[26]

The final differential momentum spectrum for protons in the vertical direction plotted from the data of Table III is shown in Fig. 7. The solid curve in Fig. 7 is the result of a Monte Carlo nucleon cascade calculation for our altitude, 747

TABLE III. Proton intensities at mountain altitude (747 g/cm^2).

Velocity interval	Momentum interval (GeV/c)	P_{av} (GeV/c)	N_p	I_p [cm^{-2}sec^{-1}sr^{-1}(GeV/c)$^{-1}$]
$0.20<\beta\leq0.35$	0.20–0.35	0.31	113	$1.49\pm1.12\times10^{-3}$ [a]
$0.35<\beta\leq0.50$	0.35–0.54	0.44	518	$9.37\pm2.25\times10^{-4}$ [a]
$0.50<\beta\leq0.60$	0.54–0.70	0.60	646	$1.14\pm0.18\times10^{-3}$ [a]
$0.60<\beta\leq0.65$	0.70–0.80	0.73	399	$1.14\pm0.09\times10^{-3}$
$0.65<\beta\leq0.70$	0.80–0.92	0.84	547	$1.21\pm0.09\times10^{-3}$
$0.70<\beta\leq0.75$	0.92–1.06	0.96	564	$9.45\pm0.66\times10^{-4}$
$0.75<\beta\leq0.80$	1.06–1.26	1.12	541	$6.58\pm0.47\times10^{-4}$
$0.80<\beta\leq0.85$	1.26–1.51	1.32	585	$4.87\pm0.36\times10^{-4}$
$0.85<\beta\leq0.90$	1.51–1.94	1.63	537	$2.68\pm0.23\times10^{-4}$
$0.90<\beta\leq0.95$	1.94–2.86	2.05	320	$1.22\pm0.21\times10^{-4}$ [b]

[a] Corrected for magnetic-field decay effects as described in text.
[b] Corrected for triggering selection effects as described in text.

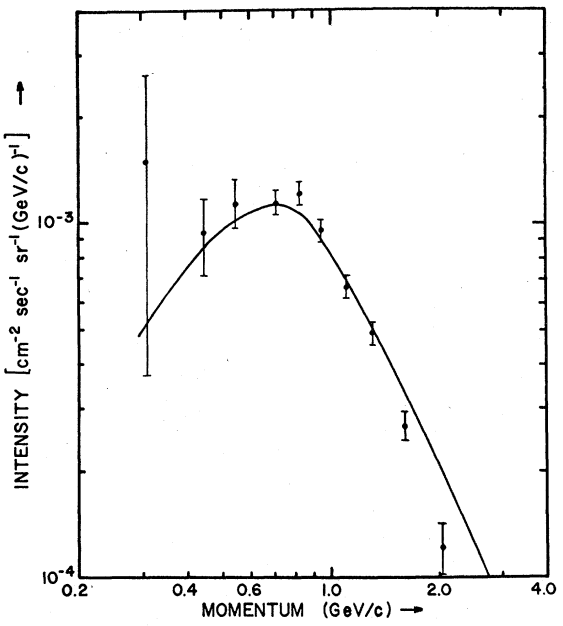

FIG. 7. Proton vertical differential momentum spectrum at mountain altitude (747 g/cm^2). The data is from this experiment. The solid curve is from the atmospheric cascade Monte Carlo calculation discussed in Appendix B.

g/cm^2, and vertical cutoff rigidity, 5.59 GV, which is discussed in Appendix B. The agreement between the Monte Carlo calculation and the experimental result is impressive when one considers that no adjustments were made in absolute intensity nor shifts in momentum to achieve this fit. The two highest-momentum experimental points fall slightly below the Monte Carlo curve, and this is perhaps due to not including enough of the high-mass tail of the proton peak in the determination of N_p (see Figs. 6(i) and 6(j). Also, the lowest-momentum point may have a systematic error not included in the error bar due to positioning of the counter $S1$ and $S2$ with respect to the magnet in the bend-angle direction. At the lowest momentum, only very small areas of counters $S1$ and $S2$ contribute to $A\Omega(p)$; a 3-cm shift of position of $S1$ or $S3$ would cause a 50% change in the rate for the lowest-momentum interval.

Deuterons

Comparison of the proton peaks in Figs. 6(a)–6(j) with proton peaks in similar histograms for the uncut data used in the determination of the proton spectrum yielded a velocity-independent survival factor $\epsilon = 0.35$ for the fraction of events surviving the additional cuts. The number of deuterons in each velocity interval containing a deuteron peak for the cut data (Fig. 6) was found after subtraction of the background by comparison of the $Q=+1$ and $Q=-1$ histograms for $M/|QM_p| = 2$. This deuteron number N_d, is shown in Table IV. The deuteron vertical differential momentum intensity was found from an equation similar to Eq. (7):

$$I_d = \frac{N_d}{\Delta p\, A\Omega(p) \Delta t_s \eta \epsilon}\,, \tag{8}$$

in a manner exactly similar to that for protons. The results are displayed in Table IV and plotted as the data points in Fig. 8.

The solid curves in Fig. 8 are the predictions of an adaptation of the Monte Carlo atmospheric cascade calculation described in Appendix B. This calculation assumes production of deuterons by the secondary cosmic-ray nucleon component in interactions of the form

$$N + A \rightarrow A' + d + \pi\,, \tag{9}$$

$$N + A \rightarrow A'' + N' + d\,, \tag{10}$$

where N and N' represent nucleons and A is the target air nucleus.

Reaction (9), which we designate a quasifree production, is analogous to the pion production reaction

$$p + p \rightarrow \pi^+ + d\,. \tag{11}$$

The cross section of reaction (11) peaks at an in-

TABLE IV. Deuteron intensities at mountain altitude (747 g/cm^2).

Velocity interval	Momentum interval (GeV/c)	P_{av} (GeV/c)	N_d	I_d [cm^{-2}sec^{-1}sr^{-1}(GeV/c)$^{-1}$]
$0.35 < \beta \leq 0.50$	0.70–1.08	0.89	10	$1.93 \pm 0.73 \times 10^{-5}$
$0.50 < \beta \leq 0.60$	1.08–1.41	1.24	8	$1.57 \pm 0.64 \times 10^{-5}$
$0.60 < \beta \leq 0.65$	1.41–1.60	1.50	3	$0.98 \pm 0.60 \times 10^{-5}$
$0.65 < \beta \leq 0.70$	1.60–1.84	1.72	7	$1.79 \pm 0.75 \times 10^{-5}$
$0.70 < \beta \leq 0.80$	1.84–2.50	2.17	1	$\leq 3.52 \times 10^{-6}$ [a]

[a] 90%-confidence upper limit assuming Poisson statistics.

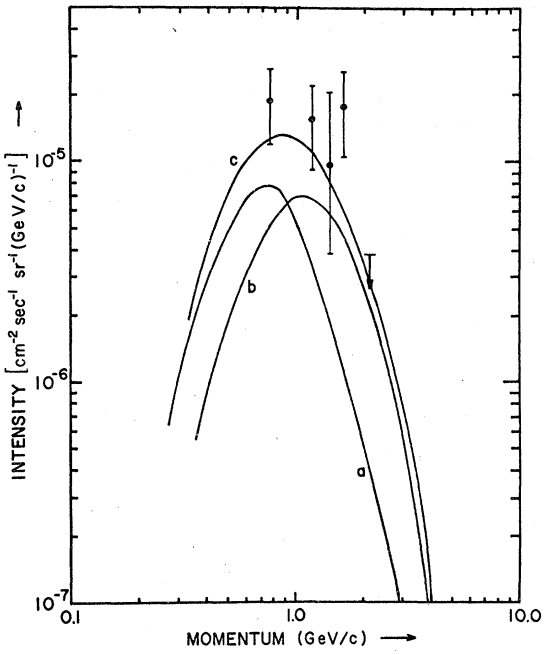

FIG. 8. Deuteron vertical differential momentum spectrum at mountain altitude (747 g/cm^2). The data is from this experiment. The solid curves are from the atmospheric cascade Monte Carlo calculation (discussed in Appendix B) and adapted for deuteron production as discussed in the main text; (a) quasifree production contribution, (b) quasielastic scattering contribution, and (c) sum of (a) and (b).

cident proton momentum near 1 GeV/c with a relatively large total cross section $\sigma(pp \to \pi^+ d) \cong 3.3$ mb.[29,30] Abundant accelerator data exist for the quasifree production process [reaction (9)] utilizing various target nuclei.[31-34] All these authors point out that

$$\frac{(d\sigma/d\Omega)(NA \to \pi A' d)}{(d\sigma/d\Omega)(pp \to \pi^+ d)} = kA^{1/3}, \tag{12}$$

where k is approximately constant for a wide range of target nuclei, of atomic number A, and over a large range of angles. Equation (12) indicates that the cross-section ratio is proportional to the nuclear radius, and thus to the circumference of the target nucleus. This implies a basically peripheral process in which the incoming nucleon interacts with a peripheral nucleon producing a pion and a deuteron with the rest of the target nucleus acting as a spectator; hence, the designation quasifree production. Presumably, nucleon shadowing and the short mean free path of the deuteron in nuclear matter prevent any sizable contribution of the nonperipheral target nucleons to this process. The numerical results of Azhgirei *et al.* as communicated by Komarov[34] are consistent with $kA^{1/3} = 1.89$ in Eq. (12), for $A = 14.5$. Reaction (9) was then assumed to be composed of two equal components directly forward and backward in the center-of-mass system so that the results could be utilized in a one-dimensional cascade calculation. Equal cross sections were assumed for incoming protons and neutrons. The total cross section for reaction (9) was then found to be

$$\sigma(NA \to \pi d A') = 1.89\sigma(pp \to \pi^+ d), \tag{13}$$

where A is an air nucleus. The Monte Carlo calculation took the Fermi momentum of the target nucleons into account by assuming that a single longitudinal component of Fermi momentum p_f was proportional to $\exp(-P_f^2/2M_\pi^2)$, where $M_\pi = 140$ MeV/c. Consideration of the Fermi momentum is particularly important in cases such as reaction (9) where the sharp peak in the cross section, as a function of momentum, of the analogous reaction (11) is substantially broadened by the intranuclear motion.

Reaction (10), which we designate quasielastic scattering, has also been well studied for various different target nuclei at accelerators.[31,33-35] Sutter *et al.*[31] and Komarov[34] point out that

$$\frac{d\sigma}{d\Omega}(NA \to N'A''d) \Big/ \frac{d\sigma}{d\Omega}(pd \to dp) \propto A^{1/3}, \tag{14}$$

with the deuteron going in the forward hemisphere for a wide range of A. Thus, quasielastic scattering is also a peripheral process. It is essentially backward elastic scattering from a pair of nucleons at the nuclear surface with the rest of the nucleus acting as a spectator. Charge exchange may also take place. A total cross section for reaction (10) with the deuteron recoiling forward was taken from the data of Azhgirei *et al.* as communicated by Komarov[34] and others[36-38] to be

$$\sigma(NA \to N'A''d) = 7.51\sigma(pd \to dp), \tag{15}$$

where $A = 14.5$ is an air nucleus.

The resultant cross sections for reactions (9) and (10) as a function of energy were inserted separately into an atmospheric cascade calculation adapted from that discussed in Appendix B. These calculations included deuteron ionization energy loss as well as deuteron removal by interaction with air nuclei. As can be seen from Fig. 8, the measured deuteron vertical differential momentum spectrum seems reasonably well accounted for by the combination of reactions (9) and (10). Other possible processes such as pickup reactions, nuclear fragment evaporation processes, and direct nuclear reactions are not expected to contribute significantly in this momentum re-

gion.

Ashton, Edwards, and Kelly[1] have published experimental results for the vertical intensity of deuterons in sea level secondary cosmic rays, but have found their results at variance with the predictions of a simple one-dimensional diffusion equation calculation which assumed deuteron production by reaction (9) alone. The two data points of Ashton *et al.*[1] for deuterons are shown in Fig. 9 together with the prediction of our atmospheric cascade calculation for the deuteron differential momentum spectrum at sea level due to the combination of reactions (9) and (10). The lower-momentum point is only about 1.5 standard deviations above the solid curve, so that agreement between our atmospheric cascade calculation and the experimental result of Ashton *et al.*[1] seems acceptable. Our calculation differs from that of Ashton *et al.*[1] in the inclusion of reaction (10), which they suggested but did not include, and in including the effect of nucleon Fermi motion in reaction (9).

Beauchamp *et al.*[15] have pointed out that deuterons of momentum near 1 GeV/c constitute a significant background source for their charge-sensitive cosmic-ray quark search for assumed-charge $\frac{4}{3}$ quarks. This should also be true for other experiments of the same genre. A precise understanding of the atmospheric deuteron secondary spectrum may now allow better upper limits to be set in these cosmic-ray quark searches.

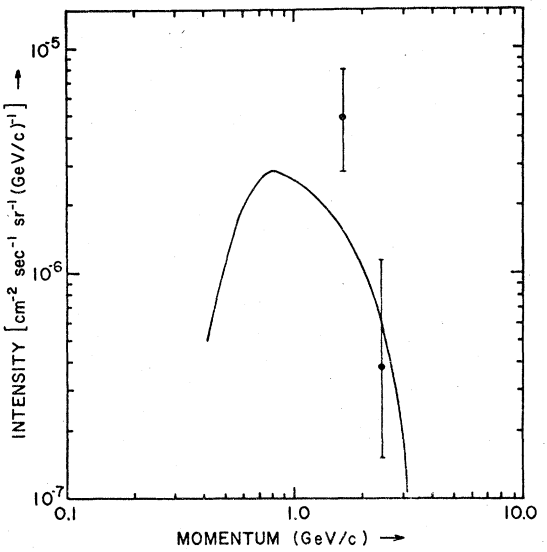

FIG. 9. Deuteron vertical differential momentum spectrum at sea level. Data are from Ashton *et al.* (Ref. 1). Solid curve is the result of the atmospheric cascade calculation described in the text.

^{4}He, ^{3}He, and ^{3}H

The number of ^{4}He (α particles) can be obtained by adding the number of particles in the peaks near $M/|QM_P| = 2$ for $Q = +2$ in Fig. 6 after subtraction of the background from $Q = -2$ and an adjustment for spillover from the $Q = +1$ deuteron peak due to statistical error in the charge determination. The number of spillover α events, column five of Table V, is determined by multiplying the ratio of the number of proton spillover events, $M/|QM_P| \cong 1$ and $Q = +2$, to the number of events in the proton peak by the number of deuterons in the deuteron peak. The resultant number of α particles is the difference between the entries in column four and column five of Table V. A statistical analysis showed that the probability of obtaining the 13 candidate α particles in the 1.39-to-3.65-GeV/c momentum interval from a Poisson-distributed spillover distribution with a mean of 4.8 was 1.4×10^{-3}. The α-particle differential momentum intensity in the vertical direction was estimated in an exactly similar manner as was done for deuterons, and the result is shown in column six of Table V.

No peaks were seen in Fig. 6 corresponding to

TABLE V. Predicted and measured intensities for light nucleii at mountain altitude (747 g/cm^2). All predictions assume production by reactions (16) and (17) only; see text.

Light nucleus	Velocity interval	Momentum interval (GeV/c)	Number observed	Predicted spillover[a]	Intensity Observed [(cm^{-2}sec^{-1}sr^{-1}(GeV/c)$^{-1}$]	Intensity Predicted [(cm^{-2}sec^{-1}sr^{-1}(GeV/c)$^{-1}$]
^{3}H	$0.35 < \beta \leq 0.70$	1.05–2.76	≤2	0	$\leq 1.9\times10^{-6}$[b]	4.98×10^{-8}[c,d]
^{3}He	$0.35 < \beta \leq 0.70$	1.05–2.76	≤2	0	$\leq 1.9\times10^{-6}$[b]	1.42×10^{-8}[c,d]
^{4}He	$0.35 < \beta \leq 0.70$	1.39–3.65	≤13	4.8	$2.2\pm1.1\times10^{-6}$	1.94×10^{-8}[d]

[a] Spillover is due to misidentification of $Q = 1$ events as $Q = 2$; see text.

[b] 90%-confidence upper limit from Poisson statistics.

[c] References used for cross sections: Bhasin and Duck,[39] Perdrisat et al.[40]

[d] References used for cross sections: Akimov, Savchenko, and Soroko[41]; Dzhelepov[32]; Komorov, Kosarev, and Savchenko[42]; Komarov.[34]

^{3}He near $M/|QM_P| = 1.5$ for $Q = +2$ or ^{3}H near $M/|QM_P| = 3.0$ for $Q = +1$. The number of possible candidates in each case for $0.20 < \beta < 0.70$ is two events. The 90% confidence limits, assuming Poisson statistics, for the ^{3}He and ^{3}H differential momentum intensity in the vertical direction at 747 g/cm^2 obtained are shown in column six of Table V.

Quasifree production and quasielastic scattering processes similar to those invoked to account for deuteron production can also be used to predict the production of ^{4}He, ^{3}He, and ^{3}H in secondary cosmic rays in the momentum region accessible to this experiment. These reactions have the form

$$N + A \rightarrow A' + a + \pi \quad \text{(quasifree production)}, \tag{16}$$

$$N + A \rightarrow A'' + a + N' \quad \text{(quasielastic scattering)}, \tag{17}$$

where N and N' are nucleons, A is the target air nucleus, a is the ^{4}He, ^{3}He, or ^{3}H produced, A' and A'' are the residual spectator nuclei, and the target in each case is now a cluster of peripheral nucleons. Charge exchange quasielastic scattering is also assumed in reaction (17).

The cross sections for the various quasielastic scattering reactions were found in a similar manner to the analogous deuteron quasielastic scattering reactions by using the results of Komarov *et al.*[42] and Komarov.[34] For quasifree production of ^{4}He, ^{3}He, and ^{3}H, the total cross section was assumed to have the same shape as reaction (9) as a function of $q = E - E_T$, where E is the center-of-mass energy and E_T is the center-of-mass energy at the pion production threshold. This is analogous to the Gaisser-Halzen[43]-type scaling discussed in the next section, except here the absolute magnitude of the cross section was scaled to the available data for pion production with light nuclei as targets[39-41] and the data for quasifree production.[32,34,42] Quasifree production cross sections for ^{3}He and ^{3}H were assumed to be identical. The cross sections were then inserted into an atmospheric cascade calculation and a separate differential momentum spectrum found for production of ^{3}He, ^{3}H, and ^{4}He by each of reactions (16) and (17). In all cases, ionization energy loss and removal of particles by collision with air nuclei was included. The quasielastic scattering and quasifree production results were then added, yielding a prediction for the differential momentum intensity in the appropriate momentum interval for each particle type (see column seven of Table V). Due to the scarcity of measurements of quasifree production of ^{4}He, the prediction for ^{4}He in Table V should be considered somewhat uncertain. However, in light of the large discrepancy between measured and predicted intensity for ^{4}He, it seems probable that some other process or processes are mainly responsible for the production of ^{4}He in secondary cosmic rays. Since ^{3}H and ^{3}He are major spallation products of ^{4}He, it is possible that the flux of these nuclei are also greatly underestimated. Alternative processes which might be important at these momenta and intensity levels are direct nuclear reactions and evaporation of fragments from excited nuclei. In any event, the cascade calculation predictions in Table V for ^{3}He and ^{3}H intensity at mountain altitude indicate that improvements to the sensitivity of this spectrometer and a longer running time should result in the observation of these components. More data for ^{4}He would also be useful to determine its spectrum.

Massive particles

As a basis for comparison in a cosmic-ray search for high-mass particles using a mass spectrometer, it is useful to calculate an upper limit for the intensity of such hypothetical particles in the cosmic-ray secondary spectrum. The differential cosmic-ray momentum spectrum for protons at the top of the atmosphere is approximated by[44]

$$I_0 = 2.0 p^{-2.75} \quad \text{for } p > 10 \text{ GeV}/c\,, \tag{18}$$

where I_0 is in units of cm^{-2} sec^{-1} sr^{-1} (GeV/c)$^{-1}$. If $\sigma(p)$ is the cross section for production of a massive particle (M) by nucleons in collisions with air nuclei (atomic number A) above a threshold incident momentum p_t, then the vertical intensity of this particle may be approximated by using the one-dimensional diffusion equation for atmospheric depth x (g/cm^2) as

$$I_M = (2.0 N_0/A)(1/\lambda - 1/\lambda_0)^{-1} \times [\exp(-x/\lambda_0) - \exp(-x/\lambda)] \int_{p_t}^{\infty} p^{-2.75} \sigma_A(p)\, dp\,, \tag{19}$$

where $N_0 = 6.024 \times 10^{23}$, and λ_0 and λ are the atmospheric attenuation mean free paths for nucleons and M particles, respectively, in g/cm^2. If we neglect shielding of nucleons by other nucleons in the nucleus and nuclear transparency to produced particle M—both of which would decrease the cross section—as well as coherent production effects which would tend to increase the cross section, we find $\sigma_A(p) \cong A\sigma_n(p)$, where $\sigma_n(p)$ is the cross section for production of M particles in nucleon-nucleon collisions at incident momentum p. Gaisser and Halzen[43] (see also

Shen and Berkeley[45]) find that the production cross sections in nucleon-nucleon collisions of two types of hadron pairs (subscripts 1,2) with spin J_k, isospin I_k, baryon number B_k, and mass M_k are related by

$$\sigma_2(Q)=\frac{2J_2+1}{2J_1+1}\frac{2I_2+1}{2I_1+1}F(B_1,B_2)\left(\frac{M_1}{M_2}\right)^2\sigma_1\left(\frac{M_1}{M_2}Q\right), \tag{20}$$

where $Q=E-E_t$, E is the center-of-mass-system (c.m.s.) energy, and E_t is the c.m.s. energy at threshold. $F(B_1,B_2)$ is a factor from quark-counting statistics of mesons and baryons [$F(1,1)=1$, $F(1,0)=6=1/F(0,1)$]. Relating the production of M-$\bar{M}$ hadron pairs to the production of p-$\bar{p}$ pairs in nucleon-nucleon interactions for which a production cross-section curve can be estimated from experimental data, we find

$$\begin{aligned} I_M &= (1.27\times 10^{24})(1/\lambda-1/\lambda_0)^{-1} \\ &\times[\exp(-x/\lambda_0)-\exp(-x/\lambda)] \\ &\times(2J_M+1)(2I_M+1)F(1,B_M) \\ &\times\frac{1}{M_M^{5.5}}\int_0^\infty\frac{\sigma_{\bar{p}}(Q)\,dQ}{Q+1.88+1.76/M_M^{4.5}}, \end{aligned} \tag{21}$$

where M_M is the M-particle mass in GeV/c^2. The results of a numerical computation are shown in Fig. 10, where $\lambda_0=120$ g/cm^2 and for simplicity M particles have been assumed to have the quantum numbers of nucleons. From Eq. (21) the generalization to other quantum numbers is obvious. Only pair production of M particles is considered here ($N+N\rightarrow N'+N''+M+\bar{M}$), but for processes analogous to associated production, a good approximation would be obtained by replacing M_M by $(M_M+M')/2$, where M' is the mass of the associated particle.

It should be noted that Fig. 10 includes M production at all momenta, whereas this experimental search is limited in momentum acceptance. The expected intensity would also be further reduced if the lifetime for M were significantly less than 10^{-6} sec. The cross-section estimate in Eq. (20) is higher and hence more optimistic for massive particle production than those obtained using statistical models of particle production with exponentially decreasing population of particle states with increasing mass.[46]

No obvious peaks or clusters of events which might be due to new particles appear in Fig. 6. Since the region of mass below twice the proton mass has been studied extensively, the most physically interesting region in this experiment is $4.0\leq M/|QM_p|\leq 10.0$ for $Q=1$ [Figs. 6(a)–6(e)] where the background is low. In the regions specified, there are two candidate events for $Q=-1$ and three for $Q=+1$. Upper limits may then be calculated under the assumption that each of the above sets of events is due to a single type of particle whose mass peak is smeared over the entire interval, a case which is somewhat worse than expected (see Appendix A).

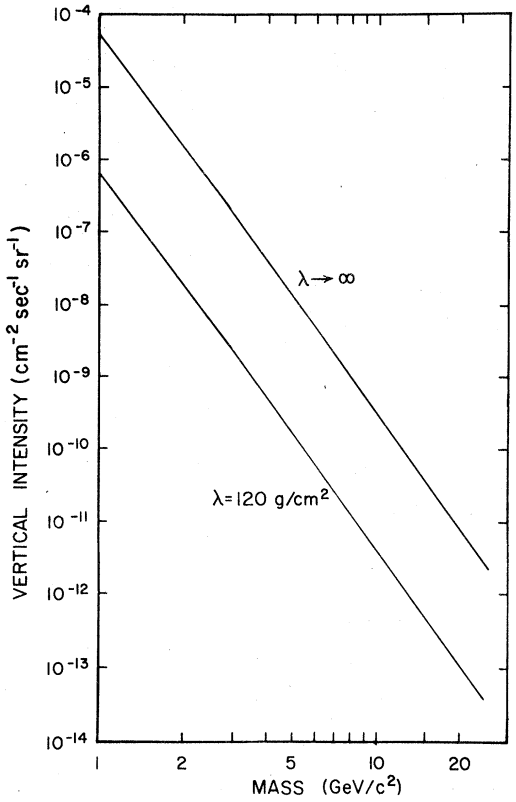

FIG. 10. Estimated integral intensity of massive particles in secondary cosmic rays at mountain altitude as a function of the particle mass for two different particle attenuation mean free paths.

Using Poisson statistics, the 90%-confidence upper limit to the vertical differential momentum intensity for each of the above cases may be found using the generalized form of Eq. (7), where the momentum is found from assuming the lowest mass in the interval. The results are shown in Table VI. Comparing these intensity upper limits with Fig. 10, it is apparent that several orders of magnitude greater sensitivity will be required before cosmic-ray data become incompatible with secondary production of hypothetical massive long-lived hadrons.

Antiprotons

Inspection of Figs. 6(a)–6(j) for $Q=-1$ reveals two low-momentum candidates for antiproton events. Comparison with adjacent mass regions discloses that these are probably not significant.

TABLE VI. Intensity upper limits for various particles at mountain altitude.

Particle charge Q	Particle	Velocity interval	Momentum interval (GeV/c)	Number of candidates	Intensity upper limit $[\text{cm}^{-2}\text{sec}^{-1}\text{sr}^{-1}(\text{GeV}/c)^{-1}]$
−1	$\bar{P}$	$0.20 < \beta \leq 0.70$	0.19–0.92	≤2	$\leq 1.08\times10^{-5}$
+1	$4M_P \leq M \leq 10M_P$	$0.20 < \beta \leq 0.70$	0.77–3.68[a]	≤3	$\leq 1.42\times10^{-6}$[a]
−1	$4M_P \leq M \leq 10M_P$	$0.20 < \beta \leq 0.70$	0.77–3.68[a]	≤2	$\leq 1.13\times10^{-6}$[a]

[a] Lower mass limit used in these calculations.

Using Poisson statistics and Eq. (8), a 90% confidence upper limit to the vertical differential momentum intensity for antiprotons is 1.1×10^{-5} $\bar{p}/\text{cm}^2$ sec sr GeV/c in the 0.19–0.92 GeV/c momentum interval (see Table VI).

Since the possible presence of a primary antiproton flux is of great astrophysical importance,[45,47-50] and evidence for primary antiprotons between 5.6 and 12.5 GeV/c has been obtained by Golden *et al.*[4] at balloon altitude, predictions for low-momentum antiproton intensities at mountain altitude are of interest. We consider the situation where the antiproton spectrum is due to secondary production by energetic protons in the atmosphere, mostly in the roughly 100-g/cm^2 thickness of air above the spectrometer. The additional antiproton intensity at mountain altitude if all of the antiprotons observed by Golden *et al.*[4] were accelerated in sources with the *same* spectrum as protons would be insignificant. If, as is more likely, antiprotons are produced by passage of cosmic rays through 5 g/cm^2 of interstellar matter, still fewer low-momentum antiprotons would be produced, and the additional antiprotons would be negligible relative to those originating in the atmosphere.

The atmospheric cascade routine employed for protons and deuterons (Appendix B) was applied to generate antiprotons with the p-p production cross sections used by Badhwar and Golden[48] increased by an $A^{2/3}$ factor for air. Antiproton scattering and annihilation cross sections were based upon the data compiled by Bracci *et al.*[51] and Enstrom *et al.*[52] The resulting predicted antiproton spectrum at 747 g/cm^2 depth is shown in Fig. 11, and has far too low an intensity to be detectable at the level of sensitivity of this experiment.

CONCLUSIONS

Cosmic-ray vertical momentum spectra have been estimated from a one-dimensional Monte Carlo calculation for protons (Figs. 7 and 13), deuterons (Figs. 8 and 9), ^{3}H, ^{3}He, and ^{4}He (Table V), and antiprotons (Fig. 11). The vertical intensity of hypothetical massive long-lived hadrons has been estimated from a one-dimensional diffusion model (Fig. 10). The proton and deuteron spectra observed in this work and by others agree well with the calculations. The upper limits obtained for the vertical intensities of ^{3}H, ^{3}He, and antiprotons are easily compatible with the calculated estimates for these components. The observed intensities of ^{4}He in the 1.4–3.7 GeV/c region were much greater than could be explained by the model employed for the Monte Carlo calculations.

ACKNOWLEDGMENTS

We thank Niels Thompson for his dedication to making the superconducting magnet a success. For their assistance in constructing and assembling various portions of the apparatus we thank Dr. Richard Rothschild, Dr. Daniel Davidson, William Black, Murdoch Gilchreise, Carl Noggle, and Orville Evans. We also thank Paul Polakos and Glen Sembroski for invaluable assistance with

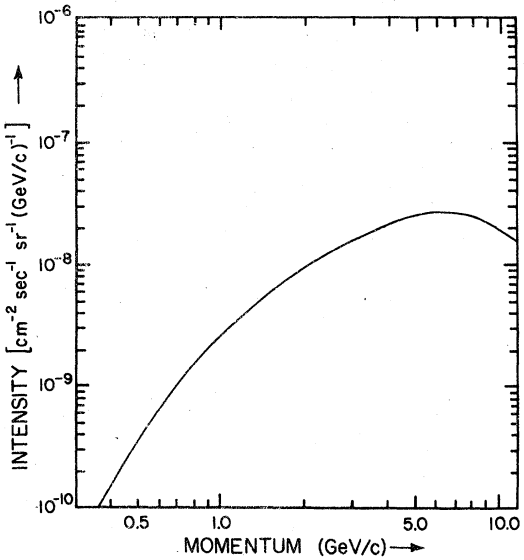

FIG. 11. Predicted differential vertical intensity for antiprotons at 747 g/cm^2 due to atmospheric secondary production.

the logistics of the experimental run. This work was supported in part by NASA Grant No. NGR03-002-071. Acknowledgment is made to the University of Arizona Computer Center for a portion of the computer time consumed by the data analysis.

APPENDIX A: MASS-RESOLUTION DETERMINATION

The standard deviation of the mass measurement, the mass resolution, due to independent random errors in the determination of bend angle, and time of flight may be found from

$$\sigma_M^2 = \left(\frac{\partial M}{\partial \theta}\right)^2 \sigma_\theta^2 + \left(\frac{\partial M}{\partial \tau}\right)^2 \sigma_\tau^2 = \left[\left(\frac{\partial M}{\partial p}\right)\left(\frac{\partial p}{\partial \theta}\right)\right]^2 \sigma_\theta^2 + \left[\left(\frac{\partial M}{\partial \beta}\right)\left(\frac{\partial \beta}{\partial \tau}\right)\right]^2 \sigma_\tau^2 . \quad \text{(A1)}$$

Using Eqs. (3) and (1b), we find

$$(\sigma_M/M)^2 = T^2 p^2 \sigma_\theta^2 + L^2 \beta^2 \gamma^4 \sigma_\tau^2 , \quad \text{(A2)}$$

where $T = 14.3\ (\mathrm{GeV}/c)^{-1}$, $L = c/Z = 0.0417\ \mathrm{nsec}^{-1}$ for T_1, and σ_θ and σ_τ are the standard deviations of measurements of the bend angle and the time of flight, respectively.

Since the velocity is determined from T_1 alone, τ is the difference between the triggering times of the two counters $S1$ and $S3$, respectively:

$$\tau = \tau_3 - \tau_1 . \quad \text{(A3)}$$

For independent random errors in τ_1 and τ_3, the standard deviation of the time-of-flight measurement becomes $\sigma_\tau^2 = \sigma_{\tau_3}^2 + \sigma_{\tau_1}^2$. Since counters $S1$ and $S3$ are of identical construction, we have $\sigma_{t_3} = \sigma_{t_1} = \sigma_t$ and $\sigma_\tau = \sqrt{2}\sigma_t$, where σ_t is the standard deviation of the measurement of the time of passage of a particle as determined by either counter. The error indicated by σ_t is mostly due to the photomultiplier tube as corrections for the light transit time in the counters have already been made.

The standard deviation of the bend-angle determination is given by

$$\sigma_\theta^2 = \sigma_{\theta_{\mathrm{MS}}}^2 + \sigma_{\theta_R}^2 , \quad \text{(A4)}$$

where σ_{θ_R} and $\sigma_{\theta_{\mathrm{MS}}}$ are the standard deviations of measurement of bend angle due to the spark-chamber resolution and multiple scattering, respectively. The spark-chamber resolution has been summarized in Table II where the bend-angle distribution for $v = c$, $I = 0$ data was used to find the maximum detectable momentum, P_{MD}, from the condition

$$\sigma_{\theta_R} \simeq \frac{0.07}{P_{\mathrm{MD}}} . \quad \text{(A5)}$$

The maximum detectable momentum obtained was $P_{\mathrm{MD}} = 31.3\ \mathrm{GeV}/c$.

Multiple Coulomb scattering in a layer of material of thickness L and radiation length L_R for a particle of velocity β, charge Q, and momentum p in GeV/c has an rms projected scattering angle

$$\sigma_{\theta_{\mathrm{MS}}} = \frac{Q(0.015\ \mathrm{GeV})}{p\beta}\left(\frac{L}{L_R}\right)^{1/2} . \quad \text{(A6)}$$

From the known characteristics of the spectrometer, the rms projected scattering angle may be found for each piece of matter in the beam path. The scattering angles then add in quadrature after being weighted by a factor $\alpha_i = (Z - Z_i)/Z$, where Z_i is the distance from the center of the magnet to either of the largest spark chambers. The result of this calculation gives the standard deviation of the bend angle due to multiple scattering as

$$\sigma_{\theta_{\mathrm{MS}}} = Q(1.62 \times 10^{-3})/p\beta . \quad \text{(A7)}$$

We can now represent the mass resolution by

$$\frac{\sigma_M^2}{M^2} = \frac{a(1)Q^2}{\beta^2} + a(2)\beta^2\gamma^2 M^2 + a(3)\beta^2\gamma^4 , \quad \text{(A8)}$$

where $a(1)$, $a(2)$, and $a(3)$, the coefficients of the multiple scattering, chamber resolution, and time-of-flight resolution terms, respectively, calculated from the preceding treatment, are shown in column three of Table VII.

TABLE VII. Comparison of mass-resolution coefficients determined by calculation and by fitting the proton-mass peak widths to Eq. (A8).

Coefficient	Term origin	Calculation	Fit to Eq. (A8)
$a(1)$	Multiple scattering	0.54×10^{-3}	$(1.06 \pm 0.14) \times 10^{-3}$
$a(2)$	Maximum detectable momentum	1.02×10^{-3} $(\mathrm{GeV}/c^2)^{-2}$	$(3.07 \pm 1.89) \times 10^{-3}$ $(\mathrm{GeV}/c^2)^{-2}$
$a(3)$	Time of flight	2.81×10^{-3}	$(2.33 \pm 0.59) \times 10^{-3}$
χ^2 of fit			3.275

If the mass-dependent second term on the right-hand side of Eq. (A8) is ignored, it may be seen that for constant velocity β and charge Q the right-hand side of Eq. (A8) is constant. Therefore, to first order, the mass resolution or width of the mass peak is proportional to the mass. This is the reason that the mass histograms of Fig. 6 were plotted on a logarithmic mass scale.

Using the logarithmic mass scale and the uncut data which was used to obtain the proton momentum spectrum in Fig. 7, a logarithmic standard deviation for the proton-mass peak for each of ten intervals of velocity was found by a maximum-likelihood fit of each peak to a Gaussian distribution. A standard deviation was then obtained for each peak, and the results are the points shown in Fig. 12. The errors are statistical and the average velocity for each point was obtained from an average of proton velocities for each velocity interval.

The solid curve in Fig. 12 is the result of a maximum likelihood fit of the mass-resolution and velocity values above to Eq. (A8) to determine the values of $a(a)$, $a(2)$, and $a(3)$. The values of σ_M for protons are plotted in Fig. 12. The fitted values of $a(1)$, $a(2)$, and $a(3)$ are shown in the fourth column of Table VII, where the error values are determined from the maximum-likelihood fit and do not include possible systematic errors introduced by the approximations used in the data reduction. However, the agreement indicated by Fig. 12 and Table VII between calculated and fitted parameters gives confidence that both the magnitude and functional dependence of the mass resolution are understood.

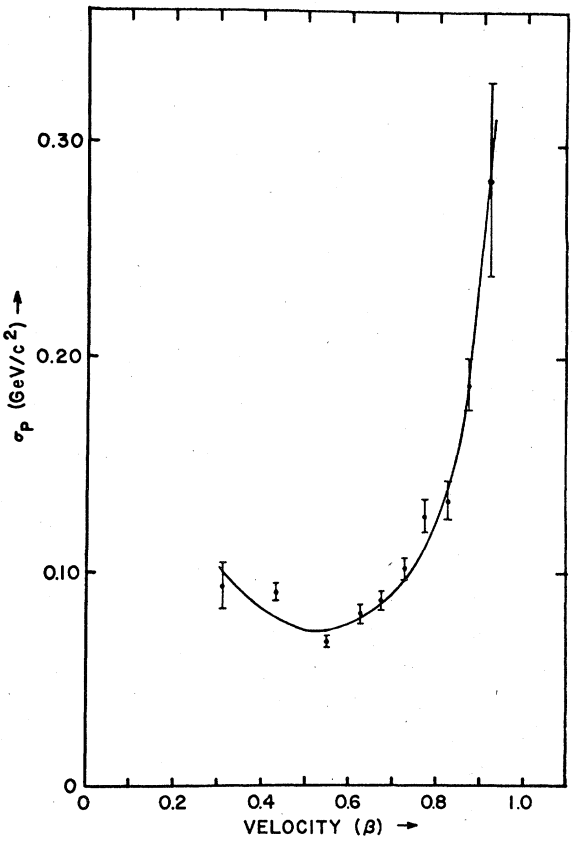

FIG. 12. Mass resolution. Data points were determined from the widths of the proton mass peaks. The solid line is a maximum-likelihood fit to Eq. (A1).

APPENDIX B: ATMOSPHERIC-NUCLEON-CASCADE SIMULATION

In order to compare the results found by this experiment both to the results of previous experiments and to theoretical predictions, it was necessary to develop a computer simulation (ATMMC), using Monte Carlo methods, of the atmospheric nucleon cascade which could model the nucleon flux at various altitudes and for various geomagnetic cutoff rigidities.

In agreement with Eq. (18), the integral primary proton momentum spectrum was taken as

$$I = 1.14 p^{-1.75} (\mathrm{cm}^{-2}\,\mathrm{sec}^{-1}\,\mathrm{sr}^{-1}), \quad p \geq 10\ \mathrm{GeV}/c\,. \tag{B1}$$

At lower momenta the spectra index was gradually lowered to 1.25 for $p \simeq 2$ GeV/c. ATMMC considers a primary flux of protons only, and the calculations are one dimensional in that only the vertical flux of both primaries and secondaries is considered. Provision is also made for truncating the incoming flux at a given momentum corresponding to the vertical cutoff rigidity for protons and rounding off the distribution near cutoff.

The interaction cross section for nucleons with air nuclei σ_{NA} was assumed independent of nucleon type, and was determined from the known data for nucleon-nucleon cross sections at various energies.[54,55] For low incoming nucleon momentum, 0.1–1.0 GeV/c, an average of the neutron-proton and proton-proton cross section was assumed; whereas above 2.0 GeV/c, the proton-proton inelastic cross section[51] was used, with the two cross sections smoothly joined in the region 1.0–2.0 GeV/c. This entire cross section was then scaled to an assumed nucleon air nucleus cross section of $\sigma_{NA} = 280$ mb at 10 GeV/c.[56,57] A mean free path was obtained from the cross section by

$$\lambda = \frac{A}{N_0 \sigma_{NA}}\ \mathrm{g/cm}^2\,, \tag{B2}$$

where $A = 14.5$ is the mean molecular weight of air and N_0 is Avogadro's number.

The nucleon-nucleus interaction is in general a complex event with a large number of possible final states. Fortunately, at high momenta the atmospheric nucleon cascade is dominated by the effects of the leading nucleon, the highest-momentum nucleon produced in the collision, due to the steeply falling momentum spectra of the nucleons producing the collisions. To preserve as much generality as possible, the following simple model was adopted for nucleon-nucleus collisions. A forward scattered nucleon was assumed with momentum:

$$p=(1-k)p_0, \quad 0\leq k\leq 1, \tag{B3}$$

where p_0 is the momentum of the nucleon producing the collision and k is called the inelasticity. The inelasticity was then given by

$$k=f_k(p_0)k_r, \tag{B4}$$

where k_r is chosen randomly from the distribution in Table VIII,[56] and $f_k(p_0)$ was a momentum-dependent factor fitted from published experimental data on cosmic-ray nucleon intensities at various altitudes (see Fig. 13).

For $p_0\geq 2$ GeV/c, $f(p_0)=1$ so that the average inelasticity is $\bar{k}\simeq 0.5$ in agreement with the usually accepted value at high energies.[54] For $p_0\leq 2$ GeV/c, $f(p_0)$ is variable between 0.5 and 1.0 to account for the differing relative importance of elastic and inelastic scattering in this momentum region.[26] Spectra obtained are not critically sensitive to choice of $f(p_0)$. The leading particle after a collision is usually a nucleon, a nuclear excited state (resonance), or another baryon, but for ATMMC it was assumed to have already decayed into a final-state proton or neutron.

The probability of a change of nucleon type (charge change) in each interaction was taken as the same for both protons and neutrons. At high momenta the incoming and outgoing leading nucleons may be of a different type, owing to the high probability of producing an excited state which then decays into several charged particles. At low momenta, charge exchange dominates the probability of change of type. The probability of a change of charge was taken as ~0.33 below 1 GeV/c and ~0.4 at higher momenta.

A recoil nucleon is also considered, whose type is chosen randomly and whose momentum is found from the kinematics, assuming backward scattering in the center of mass and the availability of a random fraction of kp_0, the laboratory momentum lost by the incoming nucleon. Momentum loss due to ionization was also included for charged particles.

The number of nucleons of each type for each of 30 momentum intervals was obtained for each of four atmospheric depths: 310 g/cm^2, 710 g/cm^2, 747 g/cm^2, and 1030 g/cm^2 (sea level).

TABLE VIII. Probability of obtaining a discrete inelasticity factor in Eq. (B4).

Inelasticity factor k_r	Probability P_r
0.15	0.033
0.25	0.067
0.35	0.167
0.45	0.233
0.55	0.233
0.65	0.167
0.75	0.067
0.85	0.033
	$\sum P_r=1.000$

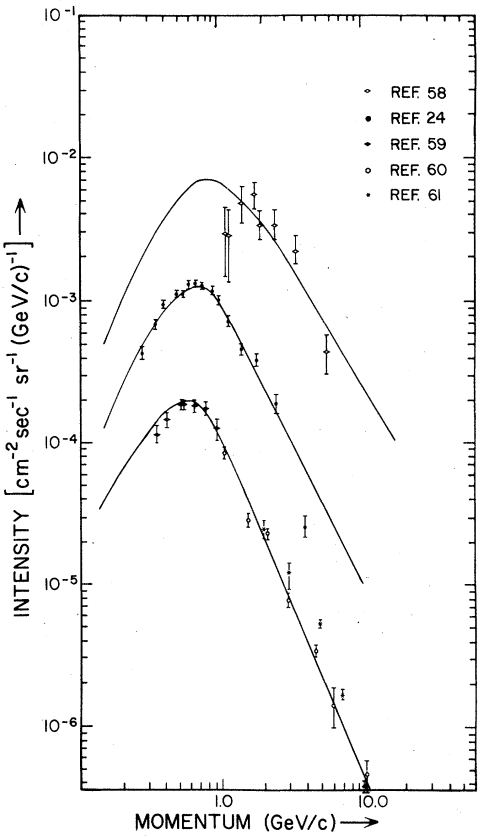

FIG. 13. Monte Carlo predictions of the proton differential momentum spectrum at three different atmospheric depths. Top curve and data of Baradzei *et al.* (Ref. 58) for 310-g/cm^2 depth, middle curve and data of Kocharian *et al.* (Ref. 24) for 710-g/cm^2 depth, bottom curve and data of Meshkovskii and Sokolov (Ref. 59), Brooke and Wolfendale (Ref. 60), and Diggory *et al.* (Ref. 61) for 1030-g/cm^2 depth (sea level).

The inelasticity parameter $f_k(p_0)$ was adjusted to obtain the best fit by eye of the nucleon cascade calculation results to the published experimental results. The resulting fit to the published results[24,58-61] for the various altitudes, shown in Fig. 13, is excellent.

Not surprisingly, the resulting proton vertical momentum spectra at high momentum determined by ATMMC are relatively insensitive to modest variations of the parameters enumerated above. This is in agreement with the fact that a relatively large number of atmospheric cascade simulations and calculations with differing parameters seem to achieve reasonable fits to the high-momentum proton spectrum.[62-65]

The complexity of ATMMC arose from the attempt to fit the turnover and low-momentum region of the vertical proton intensity using what is known about nucleon-nucleus interactions at low momenta. The dominant feature of these low-momentum interactions was the steeply rising nucleon-nucleon cross sections.

---

*Present address: ADP Network Services, Inc., 120 Broadway, Suite 2225, New York, N.Y. 10005.
†Deceased.

[1]F. Ashton, H. J. Edwards, and G. N. Kelly, in *Proceedings of the Eleventh International Conference on Cosmic Rays, Budapest, 1969,* edited by P. Gombás Acta Phys. Acad. Sci. Hung. Suppl. 29, 3 (1970) p. 327.
[2]B. Teegarden, J. Geophys. Res. 72, 4857 (1967).
[3]H. S. Bridge, H. Courant, H. de Staebler, Jr., and B. Rossi, Phys. Rev. 95, 1101 (1954); H. S. Bridge, D. O. Caldwell, Y. Pal, and B. Rossi, *ibid.* 102, 930 (1956).
[4]R. L. Golden, S. Horan, B. G. Mauger, G. D. Badhwar, J. L. Lacy, S. A. Stephens, R. R. Daniel, and J. E. Zipse, Phys. Rev. Lett. 43, 1196 (1979).
[5]L. W. Jones, D. E. Lyon, Jr., P. V. Ramana Murthy, G. DeMeester, R. W. Hartung, S. Mikamo, D. D. Reeder, A. Subramanian, B. Cork, B. Dayton, A. Benvenuti, E. Marquit, P. D. Kearney, A. E. Bussian, F. Mills, C. Radmer, and W. R. Winter, Phys. Rev. 164, 1584 (1967).
[6]S. C. Tonwar *et al.*, J. Phys. A 5, 569 (1972).
[7]S. C. Tonwar *et al.*, Pramana 8, 50 (1977).
[8]J. A. Goodman, R. W. Ellsworth, A. S. Ito, J. R. MacFall, F. Siohan, R. E. Streitmatter, S. C. Tonwar, P. R. Vishwanath, and G. B. Yodh, in *Proceedings of the Sixteenth International Cosmic Ray Conference, Kyoto, 1979* (Institute of Cosmic Ray Research, University of Tokyo, Tokyo, 1979), Vol. 6, p. 64.
[9]F. Ashton, H. J. Edwards, and G. N. Kelly, Phys. Lett. 29, B249 (1969).
[10]A. M. Galper, V. A. Gomozov, V. G. Kirillov-Ugryumov, Yu. D. Kotov, B. I. Lutchkov, and V. N. Yurov, in *Proceedings of the Twelfth International Conference on Cosmic Rays, Hobart, 1971,* edited by A. G. Fenton and K. B. Fenton (University of Tasmania Press, Hobart, Australia, 1971), p. 2317.
[11]P. C. M. Yock, Nucl. Phys. 76, B175 (1974).
[12]H. Kasha and R. J. Stefanski, Phys. Rev. 172, 1297 (1968).
[13]R. L. Fleischer, H. R. Hart, G. E. Nichols, and P. B. Price, Phys. Rev. D 4, 24 (1971).
[14]A. J. Cox, W. Beauchamp, T. Bowen, and R. M. Kalbach, Phys. Rev. D 6, 1203 (1972).
[15]W. T. Beauchamp, T. Bowen, A. J. Cox, and R. M. Kalbach, Phys. Rev. D 6, 1211 (1972).
[16]F. Ashton, in *Cosmic Rays at Ground Level,* edited by A. W. Wolfendale (Institute of Physics, London and Bristol, 1973), p. 119.
[17]M. A. Shea, D. F. Smart, and J. R. McCall, in *Proceedings of the Tenth International Conference on Cosmic Rays, Calgary, Canada, 1967,* edited by R. J. Prescott (University of Calgary, Calgary, Alberta, Canada, 1967) [Can. J. Phys. 46, S1098 (1968)].
[18]Series 8000 Spark Chamber Digitizing System, LeCroy Research Systems.
[19]NE224, Nuclear Enterprises.
[20]C. C. Low and B. Leskovar, University of California, Berkeley, Report No. UCID-3542, (EE1387), 1971 (unpublished). This tube is equivalent to the RCA 4522 utilized in our work.
[21]E. P. Krider, T. Bowen, and R. M. Kalbach, Phys. Rev. D 1, 835 (1970).
[22]C. J. Crannell and J. F. Ormes, Nucl. Instrum. Methods 94, 179 (1971).
[23]B. G. Duff, D. A. Garbutt, R. A. Rosner, and R. N. F. Walker, Nucl. Instrum. Methods 54, 132 (1967).
[24]N. M. Kocharian, G. S. Saakian, and Z. A. Korakosian, Zh. Eksp. Teor. Fiz. 35, 1335 (1958) [Sov. Phys.—JETP 8, 933 (1959)].
[25]C. J. Hume, B. C. Nandi, M. G. Thompson, M. R. Whalley, and A. W. Wolfendale, J. Phys. A 6, L73 (1973).
[26]H. B. Barber, Ph.D. thesis, University of Arizona, 1976 (unpublished).
[27]T. Bowen, W. R. Dawes, Jr., D. A. DeLise, E. W. Jenkins, J. J. Jones, R. M. Kalbach, E. I. Malamud, and D. V. Petersen, Nucl. Instrum. Methods 67, 141 (1969).
[28]W. P. Trower, *High Energy Particle Data* (Univ. of Calif. Radiation Laboratory, Berkeley, 1966), 48th ed., Vol. II (1966).
[29]M. G. Mescherjakov, N. P. Bogacer, and B. S. Neganov, Nuovo Cimento Suppl. 3, 119 (1956).
[30]D. E. Overseth, R. M. Heinz, L. W. Jones, M. J. Longo, D. E. Pellet, M. L. Perl, and F. Martin, Phys. Rev. Lett. 13, 59 (1964).
[31]R. J. Sutter, H. Palevsky, G. W. Bennett, G. J. Igo, W. D. Simpson, G. C. Phillips, D. M. Corley, N. S. Wall, and R. L. Stearns, Phys. Rev. Lett. 19, 1189 (1967).
[32]V. P. Dzhelepov, in *High Energy Physics and Nuclear Structure, Proceedings of the Third International*

Conference, Columbia University, New York, 1969, edited by S. Devons (Plenum, New York, 1970), p. 278–287.

[33]L. S. Azhgirei, Z. V. Krumshtein, Ngo Kuang Zui, V. I. Petruhkin, D. M. Hazins, and Z. Cizek, Yad. Fiz. 13, 6 (1971) [Sov. J. Nucl. Phys. 13, 3 (1971)].

[34]V. I. Komarov, Fiz. Elem. Chastits At. Yadra 5, 419 (1974) [Sov. J. Part. Nucl. 5, 168 (1974)].

[35]L. S. Azhgirei, I. K. Vzorov, V. P. Zrelov, M. G. Mescheriakov, B. S. Neganov, and A. F. Shabudin, Zh. Eksp. Teor. Fiz. 33, 1185 (1957) [Sov. Phys.—JETP 6, 911 (1958)].

[36]E. Coleman, R. M. Heinz, O. E. Overseth, and D. E. Pellett, Phys. Rev. Lett. 16, 761 (1966).

[37]S. N. Bunker, J. M. Cameron, R. F. Carlson, J. Richardson, P. Tomas, W. J. H. Van Oers, and J. W. Verba, Nucl. Phys. 113, A461 (1968).

[38]L. Dubal, C. K. Hargrove, R. J. McKee, H. Mes, L. Bird, C. Halliwell, E. P. Hincks, R. W. Morrison, J. Walters, A. C. Thompson, J. B. McCaslin, and A. R. Smith, in *High Energy Physics and Nuclear Structure, Proceedings of the Fifth International Conference, Uppsala, Sweden, 1973,* edited by G. Tibell (North-Holland, Amsterdam/American Elsevier, New York, 1974), p. 209.

[39]V. S. Bhasin and I. M. Duck, Phys. Lett. 46, B309 (1973).

[40]C. F. Perdrisat, W. Dollhopf, C. Lunke, W. K. Roberts, P. Kitching, W. Colsen, and J. R. Priest, in *High Energy Physics and Nuclear Structure, Proceedings of the Fifth International Conference, Uppsala, Sweden, 1973* (Ref. 38), p. 285.

[41]Yu. K. Akimov, O. V. Savchenko, and L. M. Soroko, Zh. Eksp. Teor. Fiz. 41, 708 (1961) [Sov. Phys.—JETP 14, 512 (1962)].

[42]V. I. Komarov, G. E. Kosarev, and D. V. Savchenko, Yad. Fiz. 11, 711 (1970); 12, 1229 (1970) [Sov. J. Nucl. Phys. 11, 399 (1970); 12, 675 (1971)].

[43]T. K. Gaisser and F. Halzen, Phys. Rev. D 11, 3157 (1975).

[44]M. J. Ryan, J. F. Ormes, and V. K. Balasubrahmanyan, Phys. Rev. Lett. 28, 985 (1972).

[45]C. S. Shen and G. B. Berkey, Phys. Rev. 171, 1344 (1968).

[46]R. Hagedorn, lectures given in the Academic Training Program of CERN, 1970–1971, Report No. CERN 71-12, 1970, p. 106 (unpublished).

[47]J. R. Wayland and T. Bowen, Phys. Rev. 171, 1376 (1968).

[48]G. D. Badhwar and R. L. Golden, Nature 151, 126 (1974).

[49]T. K. Gaisser and E. H. Levy, Phys. Rev. D 10, 1731 (1974).

[50]S. N. Ganguli and B. V. Sreekantan, in *Proceedings of the Fourteenth International Conference on Cosmic Rays, Munich, 1975,* edited by Klaus Pinkau (Max-Planck-Institut, München, 1975), Vol. 2, p. 570.

[51]E. Bracci, J. P. Droulez, E. Flaminio, J. E. Hansen, and D. R. O. Morrison, CERN High-Energy Reactions Group, Report No. CERN/HERA 73-1, 1973 (unpublished).

[52]J. E. Enstrom, T. Ferbel, P. F. Slattery, B. L. Werner, Z. G. T. Guiragossian, Y. Sumi, and T. Yoshida, Particle Data Group, Report No. LBL-58, Lawrence Berkeley Laboratory, 1972 (unpublished).

[53]D. H. Perkins, *Introduction to High Energy Physics* (Addison-Wesley, Menlo Park, California, 1972), p. 33.

[54]S. Hayakawa, *Cosmic Ray Physics Nuclear and Astrophysical Aspects* (Wiley, New York, 1969), p. 177–178.

[55]Particle Data Group, Phys. Lett. 50B, 1 (1974).

[56]E. L. Feinberg, Phys. Lett. Suppl. 5C, 5 (1972).

[57]J. C. Sens, Ann. N.Y. Acad. Sci. 229, 155 (1974).

[58]L. T. Baradzei, M. V. Solov'ev, Z. I. Tulinova, and L. I. Filatova, Zh. Eksp. Teor. Fiz. 36, 1617 (1959) [Sov. Phys.—JETP 9, 1151 (1958)].

[59]A. G. Meshkovskii and L. I. Sokolov, Zh. Eksp. Teor. Fiz. 33, 542 (1957) [Sov. Phys.—JETP 6, 424 (1958)].

[60]G. Brooke and A. W. Wolfendale, Proc. Phys. Soc. London 83, 843 (1964).

[61]I. S. Diggory, J. R. Hook, I. A. Jenkins, and K. E. Turver, J. Phys. A 7, 741 (1974).

[62]A. Jabs, Z. Phys. 212, 222 (1968); Nuovo Cimento 12, A569 (1972).

[63]K. Pinkau, Fortschr. Phys. 12, 139 (1969).

[64]K. O'Brien, Nuovo Cimento 3, A521 (1971).

[65]J. R. Hook and K. E. Turver, J. Phys. A 7, A765 (1974).